Samuel M. Smith[1]
Cavitation Research Laboratory,
Australian Maritime College,
Launceston 7248, Tasmania, Australia,
e-mail: ssmith18@utas.edu.au

James A. Venning
Cavitation Research Laboratory,
Australian Maritime College,
Launceston 7248, Tasmania, Australia

Dean R. Giosio
Cavitation Research Laboratory,
Australian Maritime College,
Launceston 7248, Tasmania, Australia

Paul A. Brandner
Professor
Cavitation Research Laboratory,
Australian Maritime College,
Launceston 7248, Tasmania, Australia

Bryce W. Pearce
Cavitation Research Laboratory,
Australian Maritime College,
Launceston 7248, Tasmania, Australia

Yin L. Young
Professor
Department of Naval Architecture and Marine Engineering,
University of Michigan,
Ann Arbor, MI 48109

Cloud Cavitation Behavior on a Hydrofoil Due to Fluid-Structure Interaction

Despite recent extensive research into fluid–structure interaction (FSI) of cavitating hydrofoils, there remain insufficient experimental data to explain many of the observed phenomena. The cloud cavitation behavior around a hydrofoil due to the effect of FSI is investigated, utilizing rigid and compliant three-dimensional (3D) hydrofoils held in a cantilevered configuration in a cavitation tunnel. The hydrofoils have identical undeformed geometry of tapered planform with a constant modified NACA0009 profile. The rigid model is made of stainless steel and the compliant model of a carbon and glass fiber-reinforced epoxy resin with the structural fibers aligned along the spanwise direction to avoid material bend-twist coupling. Tests were conducted at an incidence of 6 deg, a mean chord-based Reynolds number of 0.7×10^6 and cavitation number of 0.8. Force measurements were simultaneously acquired with high-speed imaging to enable correlation of forces with tip bending deformations and cavity physics. Hydrofoil compliance was seen to dampen the higher frequency force fluctuations while showing strong correlation between normal force and tip deflection. The 3D nature of the flow field was seen to cause complex cavitation behavior with two shedding modes observed on both models. [DOI: 10.1115/1.4042067]

1 Introduction

The fluid–structure interaction (FSI) characteristics of flow over a lifting body can significantly affect the performance of maritime propulsion and control systems. Recent research into the development of composite propellers [1–3] and active control surfaces [4,5] has taken place to exploit the ability to passively tailor geometric aspects of the hydrofoil such as skew and pitch based on the loading distribution [6]. Not only does this self-adaptive behavior give the ability to design a more energy efficient propeller, but also delay and mitigate the adverse effects of cavitation. One of these effects is the unsteady loading and induced vibration due to the shedding of cloud cavitation.

The effect of unsteady cloud cavitation on the hydroelastic response of hydrofoils has previously been investigated [7–12], with recently Pearce et al. [13] showing that the cavity dynamics influences the FSI response. In addition to the classical shed vortex-induced structural response in single-phase flow, there is interaction between the development of cavitation on the structural dynamics [10,11]. These effects are highlighted in numerical and experimental data by Akcabay et al. [8] and Young et al. [14], increased flexibility of an isotropic hydrofoil was seen to increase the cavity length as well as cause a reduction in the cloud cavitation shedding frequency. Further research also shows that flexibility broadens the induced vibration frequency content, potentially leading to severe vibration amplification caused by lock-in [8]. Increased vibrations also occur when the unsteady cavity closure approaches the hydrofoil trailing edge due to high amplitude load fluctuations caused by periodic shedding of sheet-cloud cavitation [8,14]. These previous investigations have focused on the resulting structural behavior without any detailed analysis undertaken of the associated cavity dynamics.

Sheet and cloud cavitation was first extensively studied by Knapp [15], observing the detachment/shedding of cloud cavitation from a sheet cavity. Since then, several mechanisms have been identified as the primary instability causing periodic shedding, depending on the conditions. These included growth of interfacial instabilities such as Kelvin–Helmholtz waves [16,17], re-entrant jet formation [18–23], and shock propagation [24–26]. In a recent study on cloud cavitation about a sphere, all three mechanisms have been observed occurring either under varying flow conditions or as a complex coupled mechanism [27].

To reduce the complexity of the cavitation dynamics, much hydrofoil cloud cavitation research limit three-dimensional (3D) effects, such as the spanwise effects shown in Fig. 1. This is highlighted in time-resolved particle image velocimetry experiments on a 3D hydrofoil by Foeth et al. [28], showing significant cavitation stability sensitivity to 3D flow effects. Spanwise variations are still observed on two-dimensional hydrofoils where the spanwise cavity length is seen to be proportional to the streamwise length [29]. This relationship can result in spanwise cavity lengths that are compatible with the hydrofoil geometry. In these instances, the shedding cloud cavitation exhibits much stronger periodicity than in other conditions [20].

In this study, force and tip displacement measurements are presented for a nominally rigid stainless steel and a flexible composite hydrofoil under conditions that cause cloud cavitation. The

[1]Corresponding author.

Contributed by the Fluids Engineering Division of ASME for publication in the Journal of Fluids Engineering. Manuscript received February 6, 2018; final manuscript received November 19, 2018; published online January 8, 2019. Assoc. Editor: Olivier Coutier-Delgosha.

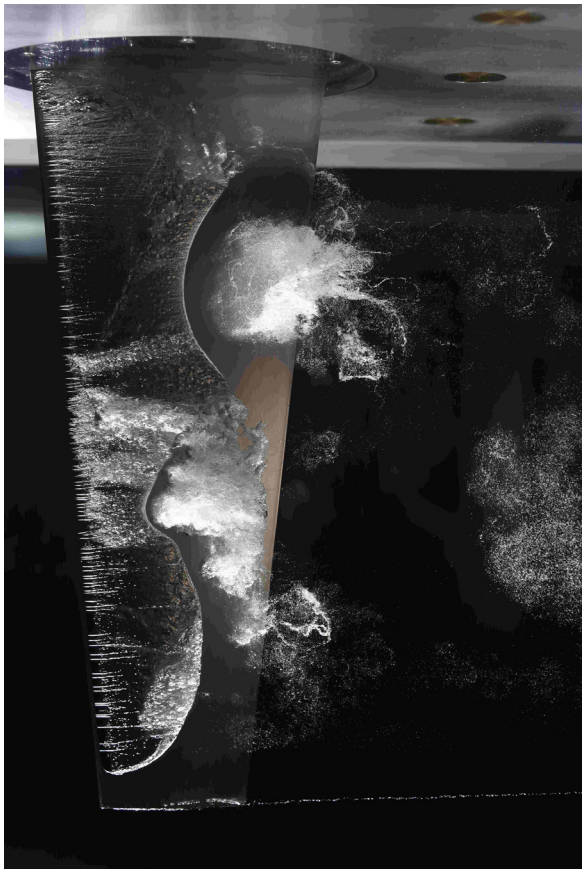

Fig. 1 Cloud cavitation about a NACA0009 stainless steel hydrofoil at $\sigma = 0.8$, $Re_c = 0.7 \times 10^6$ and $\alpha = 6$ deg

model hydrofoils are tested in identical flow conditions to permit comparison of only the flexibility/hydroelasticity effects on the cloud cavitation behavior. Synchronized high speed photography is used to analyze the cavitation behavior and assess the correlation between the cavity dynamics and forces experienced. The aim of this research is to further the understanding of cloud cavitation about a 3D hydrofoil and how FSI can influence its behavior.

2 Experimental Overview

2.1 Model Hydrofoil Details. Geometry and mechanical properties of the hydrofoil models have been selected based on modeling the static and dynamic FSI typical of propellers and control surfaces. The chosen geometry was a symmetric (unswept) trapezoidal planform of 300 mm span with a 60 mm tip and 120 mm root chord, providing an aspect ratio = 3.33. The chord length was chosen to be compatible with the mounting to the water tunnel test section and to achieve a chord based Reynolds number, $Re_c = 0.7 \times 10^6$. The unswept geometry, in conjunction with a spanwise alignment of the fiber orientation, was intentionally chosen to principally consider spanwise bending deformation only of the flexible hydrofoil. Both models have an identical modified NACA0009 section profile with a thicker trailing edge. This modification was employed for improved manufacture of the flexible composite model. The modified profile is seen to have minimal effect on the forces acting on the hydrofoil as well as the induced deformations compared to the original profile [30].

The flexible (composite) model was manufactured as a carbon/glass-epoxy hybrid structure consisting of a polyolefin scaffold core, T700 unidirectional carbon fiber and biaxial E-glass fabric used as the key structural components with an outermost fine E-glass basket weave layer to aid surface finish. A full lay-up sequence and construction procedure is detailed in Ref. [30], where the composite hydrofoil model used in the present study is termed the carbon fibre reinforced plastic (CFRP)00 hydrofoil. The rigid (stainless steel) model was machined from a Type 316 stainless steel billet with both models manufactured to ± 0.1 mm surface tolerance and 0.8 μm surface finish.

The response spectra of both hydrofoils was determined from both impact tests and hydrofoil loading spectra [30]. First mode natural frequencies were obtained in air at 96 Hz and 112 Hz, and in water at 54 Hz and 40 Hz for the stainless steel (rigid) and composite (flexible) models, respectively.

2.2 Experimental Setup. Measurements were carried out in the Cavitation Research Laboratory water tunnel at the Australian Maritime College. The tunnel test section is 0.6 m square by 2.6 m long in which the operating velocity and pressure ranges are 2–12 m/s and 4–400 kPa absolute, respectively. The tunnel volume is 365 m^3 with demineralized water (conductivity of order 1 μS/cm). The test section velocity is measured from one of two (high and low range) Siemens Sitransp differential pressure transducers models, 7MF4433-1DA02-2AB1-Z and 7MF4433-1FA02-2AB1-Z (measuring the calibrated contraction differential pressure), with estimated precisions of 0.018 and 0.007 m/s, respectively. A detailed description of the facility is given in Ref. [31]. As shown in Fig. 2, two profiled plates are used to clamp the model within a housing that is attached to a six-component force balance. The hydrofoil, located at the midlength of the test section, extends vertically into the flow through a 160 mm diameter penetration in the ceiling. The penetration is made fair (to 50 μm) using a disk mounted on the measurement side of the balance. The fairing disk has a 0.5 mm radial clearance to avoid interference with the force measurement.

2.3 Experimental Techniques. Data were obtained for a cavitation number, σ, of 0.8 and at a freestream velocity, U_∞, of 8.5 m/s, which corresponds to a $Re_c = 0.7 \times 10^6$, with the models at an incidence, α, of 6 deg. The cavitation number is defined as $\sigma = 2(p - p_v)/\rho U_\infty^2$ and Reynolds number as $Re_c = U_\infty c/\nu$, where p is the static pressure at the test section centerline, p_v is the vapor pressure, ρ is the water density, c is the mean chord, and ν is the kinematic viscosity of the water. Of the total load vector measured, only the time-varying component of the normal force is presented. The force balance was calibrated by a least squares fit between a basis vector loading cycle and the six outputs giving a 6×6 matrix. An estimated uncertainty on all components is less than 0.1%.

The cavitation behavior was recorded using high-speed photography with a HighSpeedStar8 (LaVision, Göttingen, Germany) mounted on the side of the test section. The camera was outfitted with a Nikkor f/1.4 50 mm lens and setup with a magnification factor of 3.28 px/mm. High-speed images were recorded with a spatial resolution of 1024×1024 at 7000 Hz for the rigid hydrofoil, where the flexible foil was recorded at 1000 Hz. The lower frame rate used for the composite hydrofoil was imposed by the system setup to allow synchronized acquisition with a second high-speed camera for defection measurement (as described later).

The force data for the stainless steel model were found to be nominally invariant with Reynolds number for $\alpha \leq 6$ deg. On this basis, unsteady tip bending displacement, δ'_{tip}, was only recorded for the flexible model with measurements achieved by tracking 2.3 mm diameter white dots on the tip of the hydrofoil. Further information on the technique used in similar experiments can be found in Ref. [5]. Tip bending displacement measurements were achieved using a HighSpeedStar5 high-speed camera mounted on the bottom of the test section. The camera was outfitted with a Nikkor *f*/1.4 105 mm lens, where images had a magnification factor of 13.38 px/mm. Images were recorded at 1000 Hz with a spatial resolution of 512×1024.

The high-speed photography was synchronized with the force measurement acquisition by simultaneous triggering from a BNC

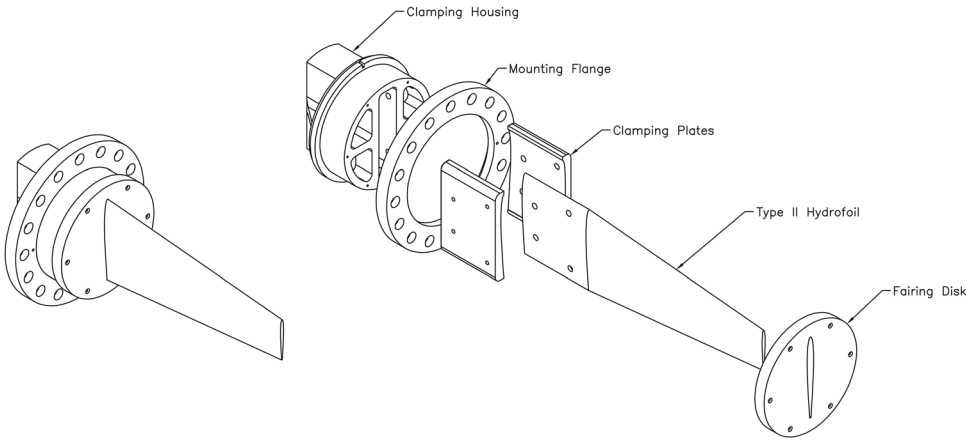

Fig. 2 Hydrofoil model assembly showing an exploded view of the clamping housing arrangement allowing continuity of the reinforcing fibers for the CFRP models [30]

model 575 Pulse Generator. Force data for the rigid and flexible hydrofoils were acquired at 7000 and 1000 Hz, respectively, to allow for comparison with the synchronized high-speed images. Tunnel flow data were acquired at 1000 Hz as this is more than sufficient to resolve the relatively large time scales and obtaining mean data.

3 Results and Discussion

The induced tip bending, δ_{tip}, and twist, θ, deformations of both the model hydrofoils have previously been measured by Zarruk et al. [30] in noncavitating flow conditions. A summary of the measurements is presented in Table 1 with interpolated values calculated at the flow speed of the current experiment shown in bold. The interpolated values were determined by fitting a second-order polynomial with a zero intercept to the data, with all R-squared values greater than 0.9994. Negligible twist was observed on the rigid model by Zarruk et al. [30].

The flexible model is seen to exhibit positive twist when loaded, estimated to be 0.309 deg at the 8.65 m/s flow speed in these experiments. This twist behavior was observed to increase the lift force of the composite hydrofoil [30] compared to the stainless steel model, indicating a change in the pressure field over the model. The change in the pressure field due to the deformations is likely to influence the cavitation behavior, particularly toward the tip where deformations are large.

3.1 Force and Tip Displacement Time Series. The normal force, X, is presented as a dimensionless coefficient, $C_X = 2X/(\rho A U_\infty^2)$, where A denotes the planform area. The frequency content of the X force experienced by either hydrofoil is shown in the power spectral density in Fig. 3. Both hydrofoils exhibit a common primary frequency at approximately 37 Hz, with secondary frequencies at 49 and 42 Hz for the rigid and flexible hydrofoils, respectively. The common fluctuation at 37 Hz is linked to periodic shedding of cloud cavitation from the top half of the hydrofoils, as made evident in space-time diagrams discussed later. These plots also reveal another shedding mechanism toward the tip of the rigid hydrofoil fluctuating at approximately 49 Hz, explaining the secondary peak. Coupling between the dynamic response of the flexible hydrofoil and the unsteady cloud cavitation is linked to the 42 Hz peak. The slight rise in natural frequency, compared to that in Table 2, is attributed to reduction in added mass due to the presence of vapor cavities.

Figures 4 and 5 show a short time series of C_X, the unsteady tip bending displacement to chord ratio, δ'_{tip}/c, and pixel intensity, I, for both the rigid and flexible hydrofoils. Pixel intensity was taken along the span, s, at $0.24s$, $0.47s$, and $0.77s$ from the root, and at $0.75c$ of the local chord for both hydrofoils. Frames taken from the synchronized high-speed video show one full shedding cycle at the dominant frequency, with the first and last frames coinciding with the maximum force of the primary frequency component. For both hydrofoils, the primary frequency corresponds to a full length cavity being shed. The maximum force occurs just after the attached cavity breaks off and a new cavity has just formed. The minimum force coincides with maximum cavity length. Pixel intensity behavior of the rigid hydrofoil exhibits a rise, plateau, and fall cycle at the middle pixel ($0.47s$) during the shedding cycle shown. The top pixel ($0.24s$) shows similar behavior and duration, but slightly trails the middle pixel intensity in time. The bottom pixel ($0.77s$) exhibits peaks for a much shorter duration

Table 1 Tip bending and twist deformation measurements [30] of the rigid and flexible hydrofoil at $\alpha = 6$ deg

	Rigid			Flexible		
$\mathrm{Re} \times 10^6$	U (m/s)	δ (mm)	θ (deg)	U (m/s)	δ (mm)	θ (deg)
0.2	2.37	0.19	—	2.35	0.53	0.0189
0.4	4.73	0.76	—	4.68	2.19	0.0801
0.6	7.10	1.75	—	7.02	5.09	0.1956
0.7	**8.65**	**2.74**	—	**8.65**	**8.15**	**0.3090**
0.8	9.43	3.14	—	9.34	9.43	0.3615
1.0	11.74	5.01	—	11.63	15.41	0.5894

Note: In noncavitating flow conditions with interpolated values (bold) at flow speed of the current experiments. Interpolated values calculated based on fitting second-order polynomial with intercept at 0. The resulting R-squared values were 0.9998 and 0.9994 for the rigid and flexible hydrofoils, respectively.

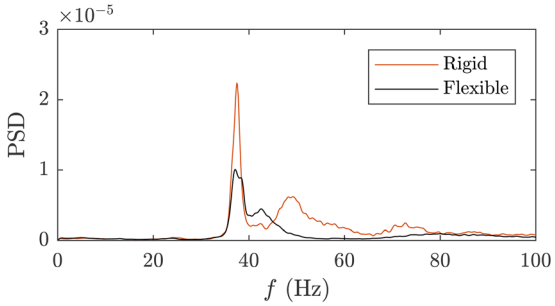

Fig. 3 Narrowband X force power spectral density for the rigid and flexible hydrofoils at $\sigma = 0.8$, $\mathrm{Re}_c = 0.7 \times 10^6$ and $\alpha = 6$ deg. The two spectra share a common peak at 37 Hz, with secondary peaks exhibited at 49 Hz and 42 Hz for the rigid and flexible hydrofoil, respectively.

Table 2 Statistics of the shedding frequency calculations determined from chordwise space-time diagrams of the rigid and flexible hydrofoil taken at 0.33*s* and 0.77*s* along the span

	Rigid		Flexible	
Shedding statistics	Top (0.33*s*)	Bottom (0.77*s*)	Top (0.33*s*)	Bottom (0.77*s*)
Shedding frequency (Hz)	37	54	37	45
Standard deviation (Hz)	3.8	4.5	3.4	5.0
Range (s)	0.021–0.031	0.017–0.022	0.023–0.032	0.018–0.028

compared to the other pixels and primarily occurs when the top (0.24*s*) and middle (0.47*s*) pixels are low. These pixel intensity traits suggest that there are two shedding modes, one covering the top and middle, and the other at the bottom of the span, that alternate and interact over time. The flexible hydrofoil shows similar trends, but due to low temporal resolution imposed by the data acquisition limitations of using the synchronized high-speed cameras, definitive conclusions cannot be made at this stage.

Comparing the force signals, the rigid hydrofoil exhibits a slightly lower mean C_X to that of the flexible hydrofoil, 0.5406 and 0.5497, respectively. This is likely due to the load-induced twist deformations of the flexible hydrofoil causing an increased pressure differential, as seen in Ref. [30]. However, the rigid hydrofoil exhibits more unsteadiness with a C_X root-mean-square (RMS) values of 0.035, compared to 0.031 for the flexible model. The unsteady tip displacement of the flexible hydrofoil is seen to vary significantly over time, having a strong correlation with C_X as expected. The trailing edge displacement exhibited greater unsteadiness than the leading edge with standard deviations of 0.43 and 0.37 mm, respectively. This can be attributed to the greater flexibility toward the trailing edge due to the geometry of the profile.

3.2 Shedding Mechanisms and Cavity Dynamics. Temporal cavitation behavior can be represented by extracting either the same row or column of pixels from each frame and placing them sequentially next to one another, as shown in Figs. 6–8. Horizontal and vertical lines have been added to Figs. 4(*c*) and 5(*c*) to indicate the locations used to obtain the space–time diagrams. In the chordwise space-time diagrams (Figs. 6 and 7), of which are taken at 0.33*s* along the span from the root, the flow direction is from the top to the bottom. In the spanwise space-time diagrams (Fig. 8), which are taken at 0.11*c* upstream of midchord, the flow direction is left to right.

Through analysis of the high-speed videos, it is evident that the primary shedding mechanism is the classical re-entrant jet. A typical shedding process can be seen in the space–time diagram of the rigid hydrofoil (Fig. 6(*a*)) generated from a line of pixels extracted at 0.33*s* from the root, shown by a horizontal dashed green line in Figs. 4(*c*) and 5(*c*). In the annotated version of the space–time diagram (Fig. 6(*b*)), a shedding cycle starts when an attached cavity near the leading edge of the hydrofoil begins to grow, with the downstream end of the attached cavity shown by the oblique solid line. As the cavity grows, it closes in a strong adverse pressure gradient region, causing a re-entrant jet to eventually form in between the foil surface and the cavity. The re-entrant jet starts to propagate forward toward the leading edge, shown by the arrows, while reducing the growth speed of the cavity indicated by the change in slope of the oblique solid line. As the re-entrant jet approaches the leading edge, the attached cavity becomes thin, and surface perturbations on either interface start to interact,

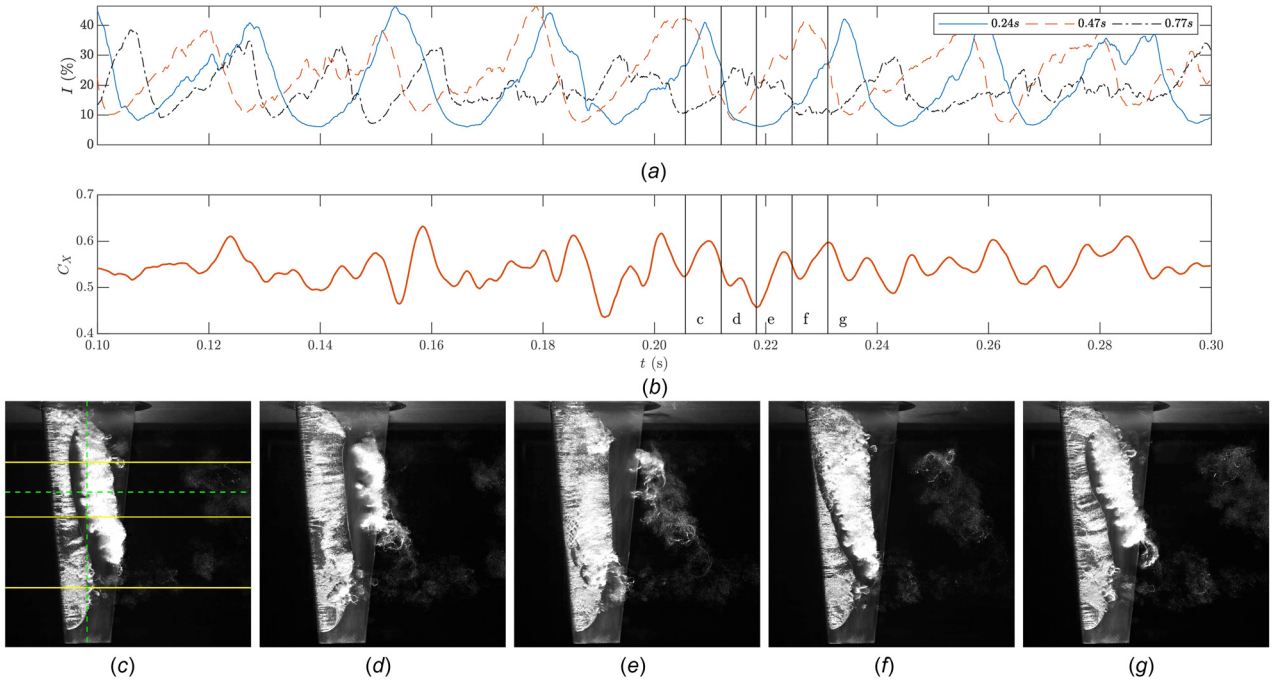

Fig. 4 Sample time series of normal force coefficient with selected images from high-speed imaging for the rigid hydrofoil. The three curves of pixel intensity are taken at 0.75*c*, for spanwise locations of 0.24*s*, 0.47*s*, and 0.77*s* from the root, as indicated by the solid lines in (*c*) and (*j*). The horizontal and vertical dashed lines in (*c*) and (*j*) indicate the position where the space-time diagrams of Figs. 6–8 were generated. Data were taken at $\sigma = 0.8$, $\mathrm{Re}_c = 0.7 \times 10^6$ and $\alpha = 6$ deg

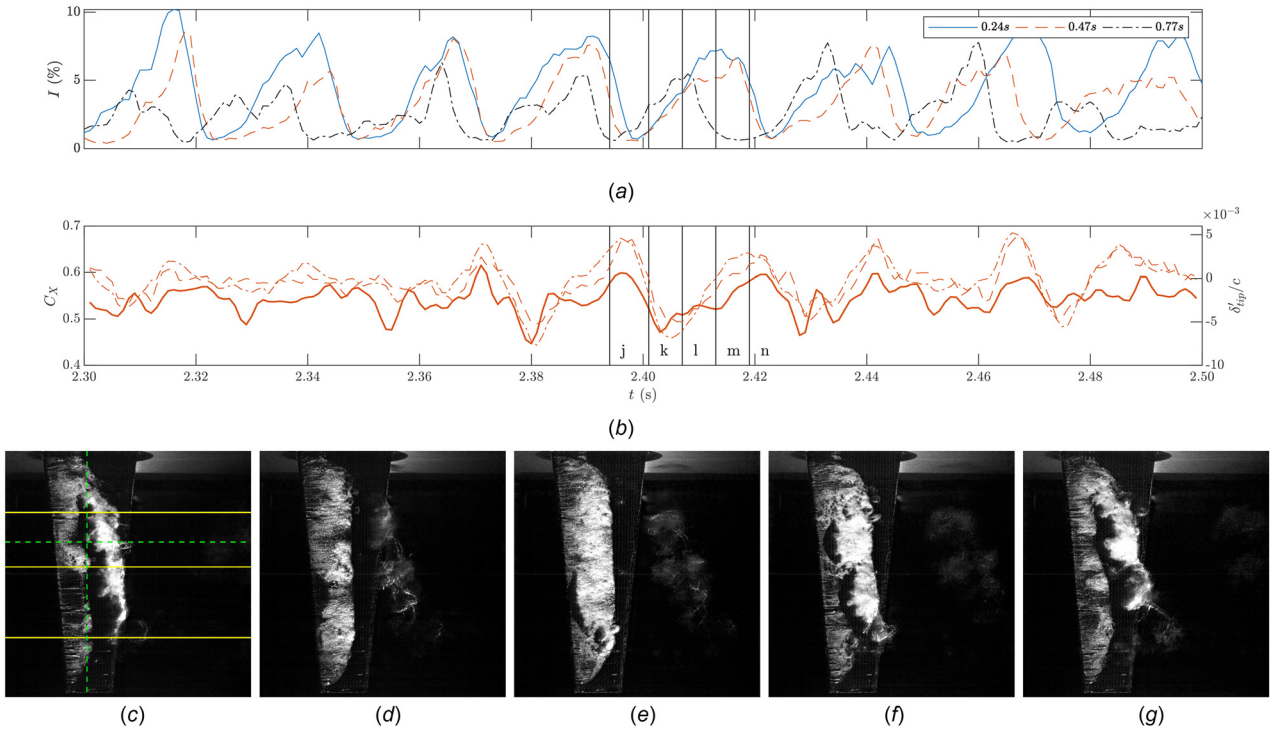

Fig. 5 Sample time series of normal force coefficient with selected images from high-speed imaging for the flexible hydrofoil. Simultaneous normalized unsteady tip bending displacement (dot-dashed line) is also presented. The three curves of pixel intensity are taken at 0.75*c*, for span-wise locations of 0.24*s*, 0.47*s*, and 0.77*s* from the root, as indicated by the yellow solid lines in (*c*) and (*j*). The horizontal and vertical green dashed lines in (*c*) and (*j*) indicate the position where the space-time diagrams of Figs. 6–8 were generated. Data were taken at $\sigma = 0.8$, $Re_c = 0.7 \times 10^6$ and $\alpha = 6$ deg.

resulting in initial partial break-up of the cavity. This is indicated by the white streaks coming off the upstream end of the re-entrant jet (solid curve). Eventually, the re-entrant jet reaches the upstream end of the attached cavity, with this point in time represented by the vertical dashed line. At this point, the cavity becomes detached from the hydrofoil surface and is then broken up in the flow, forming a chaotic cloud of small vapor structures that is advected downstream (dashed curve). This break-off of the

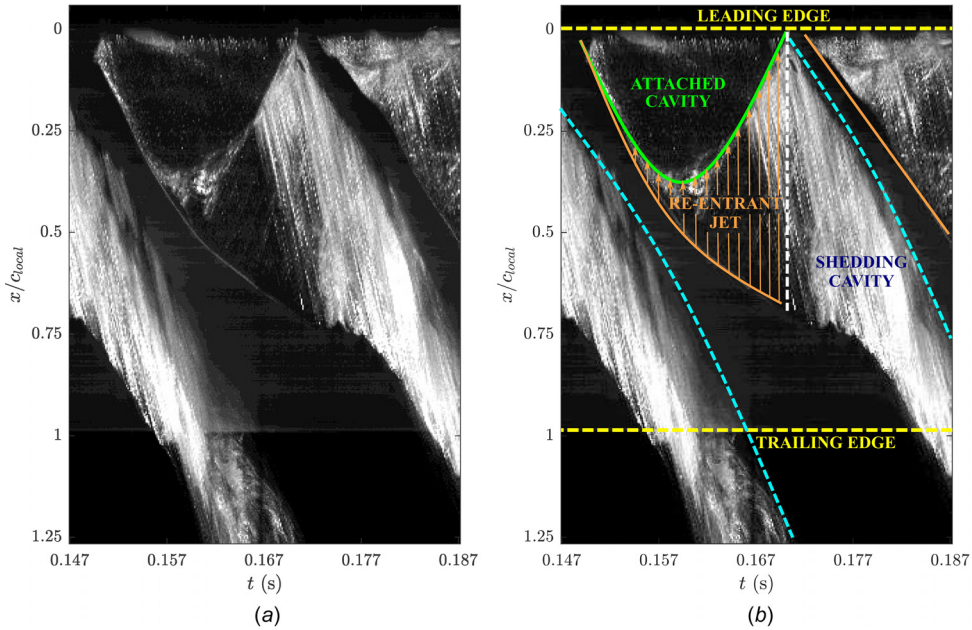

Fig. 6 Chordwise spacetime diagrams taken 0.33*s* along the span (indicated by horizontal dashed green line in Figs. 4(*c*) and 5(*c*)) of a single shedding cycle of the rigid hydrofoil. The unannotated diagram (*a*) shows a clear depiction of a single shedding cycle. The annotated diagram (*b*) shows the downstream end of the attached cavity (oblique solid line), path of the re-entrant jet (arrows) along with its upstream extent (solid curve), the point in time the cavity becomes detached (vertical dashed line), and the path of the shedding cavity (dashed curve). The space-time diagrams were taken at $\sigma = 0.8$, $Re_c = 0.7 \times 10^6$ and $\alpha = 6$ deg. The flow direction is from top to bottom

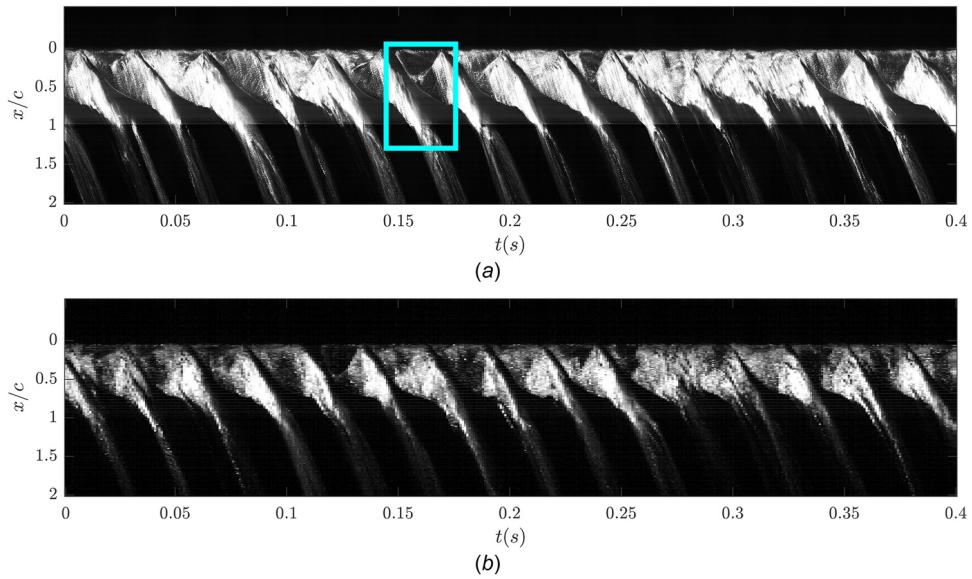

Fig. 7 Chordwise space-time diagram from high speed images taken 0.33*s* from the root (indicated by a horizontal dashed line in Figs. 4(*c*) and 5(*c*)) for the rigid (*a*) and flexible hydrofoil (*b*) at $\sigma = 0.8$, $\mathrm{Re}_c = 0.7 \times 10^6$ and $\alpha = 6$ deg. The square in (*a*) indicates the cut-out taken for the shedding mechanism diagram in Fig. 6. The flow direction is top to bottom: (*a*) rigid hydrofoil and (*b*) flexible hydrofoil

attached cavity due to the re-entrant jet leaves a clean region for a new cavity to grow, and the next shedding cycle to begin. This classic re-entrant jet shedding cycle is not always the case in the tested conditions and can vary significantly due to the complex 3D flow physics present in the experiment.

At the flow conditions examined here ($\mathrm{Re}_c = 0.7 \times 10^6$, $\sigma = 0.8$ and $\alpha = 6$ deg), the NACA0009 hydrofoil forms a relatively thin cavity, resulting in a thin jet that potentially has insufficient momentum to break through to the cavity detachment point. This is due to friction between adjacent interfaces of the cavity and the hydrofoil [19,32]. A sufficiently thin cavity may also have significant interactions between the upper and lower interfaces of the cavity as surface perturbations become predominant, leading to small-scale vapor structures being shed instead of a large-scale cloud [22]. This can be seen in chordwise space-time diagram (Fig. 7) of several shedding cycles where there is significant variation between each cycle. The interaction of surface perturbations manifests as rough opaque surfaces, seen in Fig. 7, compared to the transparent regions shown in Fig. 6. Comparison of the rigid and flexible hydrofoils reveals shedding variations over time exist for both hydrofoils but are not as severe for the flexible hydrofoil.

The spanwise space-time diagrams for both hydrofoils (Fig. 8) illustrate how the cloud cavitation varies along the span over time. It is observed that there is significant spanwise variation for both hydrofoils with no uniform (i.e., across the whole span) shedding observed. This complex cavitation behavior is due to the

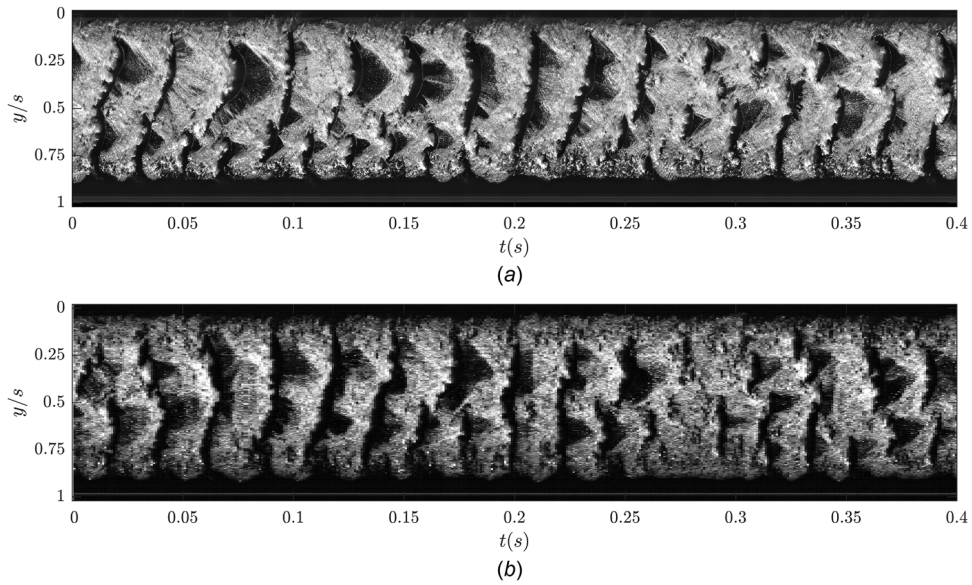

Fig. 8 Spanwise space-time diagrams from high speed images 0.11*c* upstream of the midchord (indicated by a vertical green dashed line in Figs. 4(*c*) and 5(*c*) for the rigid (*a*) and flexible hydrofoil (*b*) at $\sigma = 0.8$, $\mathrm{Re}_c = 0.7 \times 10^6$ and $\alpha = 6$ deg. The flow direction is left to right: (*a*) rigid hydrofoil and (*b*) flexible hydrofoil

interaction of multiple effects. This includes spanwise flow disparity over the hydrofoil due to the tapered 3D geometry that causes variations in the re-entrant jet propagation direction. Additionally, the nature of the vertical mounted hydrofoil results in a cavitation number gradient along the span, as well as buoyancy effects on the cavities.

A level of consistency is seen in the periodicity of shedding, but the shedding behavior of each event varies with a clear re-entrant jet observed in some, but not in others. Variation in the shedding behavior is observed in Fig. 7 by the presence, or lack of, a re-entrant jet, as depicted in Fig. 6(*b*). The cycle in which a re-entrant jet is lacking can first occur when the shedding cavity is not directly at the position of the space–time and only captures the adjacent small chaotic vapor cavities. Alternatively, a re-entrant jet may not have enough momentum to cleanly break-off the attached cavity, preventing a new cavity from forming, and thus breaking the cycle. In Fig. 8, variations between cycles are mainly evident by the size, position, and number of crescent shape cut-outs in the shedding events. Each crescent shape cut-out represents the progression of a re-entrant jet, and it can be seen that multiple jets can form along the span at any one time. Shedding at the top of the foil is characterized by larger re-entrant jet formation, with longer periodic cycles, where the tip features smaller and higher frequency jet formations.

Analysis of the rigid and flexible hydrofoil spanwise space-time diagrams (Fig. 8) reveals the existence of two shedding modes along the span. Taking the time at which each shedding cycle starts in the chordwise space–time diagrams, taken at 0.33*s* and 0.77*s* along the span, the shedding frequencies are determined with statistics presented in Table 2. The shedding frequencies at the top (0.33*s*) of either model are equal at 37 Hz, and match those observed in the *X* force power spectral density (Fig. 3). Shedding frequencies were calculated higher toward the tip of the model (0.77*s*) at 54 Hz and 45 Hz for the rigid and flexible model, respectively. This higher shedding frequency can be attributed to the shorter cavity length toward the tip of the models. The reduced cavity length, compared to the top of the hydrofoil, is due to the shorter chord at the tip of the tapered model, as well as the local σ being higher from increased hydrostatic pressure due to the vertical orientation of the model. Cycle durations of each shedding event where not consistent, as shown in Table 2, with more variation seen at 0.77*s* for both models.

Nondimensionalizing these frequencies using a cavity length-based Strouhal number, $St = fL_c/U_\infty$, where L_c is the maximum cavity length, the rigid frequencies equate to 0.33 and 0.37 for the upper and lower parts, respectively, compared to 0.33 and 0.32 for the flexible hydrofoil.

Comparing the spanwise space-time diagram, the flexible hydrofoils secondary shedding mode at the bottom does not appear to have as strong a periodicity as the rigid hydrofoil. This could be due to the force-induced tip displacement imposed by the top shedding cavity interfering with the lower shedding physics. Additionally, the pressure field difference resulting from the flow-induced twist in the flexible hydrofoil would also have significant effect on the cavitation shedding behavior. These observations coincide with frequencies present in the *X* force spectrum (Fig. 3), supporting the strong correlation between cavity dynamics and forces.

4 Conclusions

Preliminary results are presented for the effect of FSI on cloud cavitation about a hydrofoil. The normal force, unsteady tip bending displacement, and cavitation behavior were compared for a nominally rigid stainless steel and flexible composite NACA0009 hydrofoil at $\mathrm{Re}_c = 0.7 \times 10^6$, $\sigma = 0.8$ and $\alpha = 6$ deg.

The bending deformations of the flexible hydrofoil were found to dampen some of the higher frequency fluctuations in the normal force measurements while showing a strong correlation between tip displacement and normal force.

A re-entrant jet was identified as the primary shedding mechanism, showing changes in growth and jet speed at various stages in the shedding cycle. Due to the thin cavity, surface perturbations were seen to have significant interaction, sometimes resulting in small-scale vapor pockets being shed instead of large-scale cloud cavitation.

The cavitation behavior is observed to be highly complex due to the 3D nature of the flow, causing significant spanwise flow disparity. Both hydrofoils exhibited fairly consistent periodic shedding, however, still showed varying behavior between each shedding event. Two shedding modes appeared to form along the span with either hydrofoil showing two curved regions in the cavity trailing edge, typical of a re-entrant jet. This resulted in two shedding frequencies for either hydrofoil, with both having a primary frequency of 37 Hz and secondary frequencies of 54 Hz and 45 Hz for the rigid and flexible hydrofoil, respectively. These differences are attributed to force-induced deformations affecting the cavity dynamics due to changes in the flow field. This is supported by the fact that the observed shedding frequencies closely matched those present in the *X* force spectrum.

The fluid–structure interaction phenomena observed for a flexible 3D hydrofoil experiencing cloud cavitation are highly complex. This complicated behavior makes it difficult to predict the performance of real-world applications such as composite propellers and control surfaces. Further investigation into the phenomena in a wider range of conditions will allow more detailed and accurate predictions, permitting improved development of control surfaces and marine propulsors.

Acknowledgment

This project was supported by the University of Tasmania, the Defence Science and Technology Group, U.S. Office of Naval Research (Dr. Ki-Han Kim, Program Officer), ONR Global (Dr. Woei-Min Lin) through NICOP S&T and the Research Training Centre of Naval Design and Manufacturing (RTCNDM). The RTCNDM is a University-Industry partnership established under the Australian Research Council (ARC) Industry Transformation grant scheme. The authors would like to acknowledge the assistance of Mr. Steven Kent and Mr. Robert Wrigley from the Australian Maritime College for their essential help with setting up and carrying out the experiments.

Funding Data

- Australian Research Council (ARC IC140100003, Funder ID. 10.13039/501100000923).
- Office of Naval Research Global (N62909-11-1-7013, Funder ID. 10.13039/100007297).

References

[1] Young, Y. L., 2008, "Fluid-Structure Interaction Analysis of Flexible Composite Marine Propellers," J. Fluids Struct., **24**(6), pp. 799–818.

[2] Motley, M. R., Liu, Z., and Young, Y. L., 2009, "Utilizing Fluid-Structure Interactions to Improve Energy Efficiency of Composite Marine Propellers in Spatially Varying Wake," Compos. Struct., **90**(3), pp. 304–313.

[3] Young, Y. L., Motley, M., Barber, R., Chae, E. J., and Garg, N. G., 2016, "Adaptive Composite Marine Propulsors and Turbines: Progress and Challenges," ASME Appl. Mech. Rev., **68**(6), p. 060803.

[4] Turnock, S. R., and Wright, A. M., 2000, "Directly Coupled Fluid Structural Model of a Ship Rudder Behind a Propeller," Mar. Struct., **13**(1), pp. 53–72.

[5] Young, Y. L., Garg, N., Brandner, P. A., Pearce, B. W., Butler, D., Clarke, D., and Phillips, A. W., 2017, "Load-Dependent Bend-Twist Coupling Effects on the Steady-State Hydroelastic Response of Composite Hydrofoils," Compos. Struct., **189**, pp. 398–418.

[6] Young, Y. L., 2007, "Time-Dependent Hydroelastic Analysis of Cavitating Propulsors," J. Fluids Struct., **23**(2), pp. 269–295.

[7] Akcabay, D. T., and Young, Y. L., 2014, "Influence of Cavitation on the Hydroelastic Stability of Hydrofoils," J. Fluids Struct., **49**, pp. 170–185.

[8] Akcabay, D. T., Chae, E. J., Young, Y. L., Ducoin, A., and Astolfi, J. A., 2014, "Cavity Induced Vibration of Flexible Hydrofoils," J. Fluids Struct., **49**(Suppl. C), pp. 463–484.

[9] Akcabay, D. T., and Young, Y. L., 2015, "Parametric Excitations and Lock-In of Flexible Hydrofoils in Two-Phase Flows," J. Fluids Struct., **57**, pp. 344–356.

[10] Ausoni, P., Farhat, M., Escaler, X., Egusquiza, E., and Avellan, F., 2007, "Cavitation Influence on Von Karman Vortex Shedding and Induced Hydrofoil Vibrations," ASME J. Fluids Eng., **129**(8), pp. 966–973.
[11] Wu, Q., Huang, B., Wang, G., and Gao, Y., 2015, "Experimental and Numerical Investigation of Hydroelastic Response of a Flexible Hydrofoil in Cavitating Flow," Int. J. Multiphase Flow, **74**, pp. 19–33.
[12] Ducoin, A., Astolfi, J. A., and Sigrist, J., 2012, "An Experimental Analysis of Fluid Structure Interaction on a Flexible Hydrofoil in Various Flow Regimes Including Cavitating Flow," Eur. J. Mech.-B/Fluids, **36**, pp. 63–74.
[13] Pearce, B. W., Brandner, P. A., Garg, N., Young, Y. L., Phillips, A. W., and Clarke, D. B., 2017, "The Influence of Bend-Twist Coupling on the Dynamic Response of Cavitating Composite Hydrofoils," Fifth International Symposium on Marine Propulsors (SMP'17), Helsinki, Finland, June 12–15, pp. 803–813.
[14] Young, Y., Garg, N., Brandner, P., Pearce, B., Butler, D., Clarke, D., and Phillips, A., 2018, "Material Bend-Twist Coupling Effects on Cavitating Response of Composite Hydrofoils," Tenth International Cavitation Symposium (CAV2018), Baltimore, MD, May 14–16.
[15] Knapp, R. T., 1955, "Recent Investigations of the Mechanics of Cavitation and Cavitation Damage," Trans. ASME, **77**, pp. 1045–1054.
[16] Brennen, C. E., 1969, "The Dynamic Balances of Dissolved Air and Heat in Natural Cavity Flows," J. Fluid Mech., **37**(1), pp. 115–127.
[17] Avellan, F., Dupont, P., and Ryhming, I. L., 1988, "Generation Mechanism and Dynamics of Cavitation Vortices Downstream of a Fixed Leading Edge Cavity," 17th Symposium on Naval Hydrodynamics, The Hague, The Netherlands, Aug. 29–Sept. 2, pp. 1–13.
[18] Furness, S., and Hutton, S. P., 1975, "Experimental and Theoretical Studies of Two-Dimensional Fixed-Type Cavities," ASME J. Fluids Eng., (4), pp. 515–521.
[19] Le, Q., Franc, J., and Michel, J., 1993, "Partial Cavities: Global Behaviour and Mean Pressure Distribution," ASME J. Fluids Eng., **115**(2), pp. 243–243.
[20] Kawanami, Y., Kato, H., Yamaguchi, H., Tanimura, M., and Tagaya, Y., 1997, "Mechanism and Control of Cloud Cavitation," ASME J. Fluids Eng., **119**(4), pp. 788–794.
[21] Stutz, B., and Reboud, J. L., 1997, "Experiments on Unsteady Cavitation," Exp. Fluids, **22**(3), pp. 191–198.
[22] Callenaere, M., Franc, J., Michel, J., and Riondet, M., 2001, "The Cavitation Instability Induced by the Development of a Re-Entrant Jet," J. Fluid Mech., **444**, pp. 223–256.
[23] Laberteaux, K. R., and Ceccio, S. L., 2001, "Partial Cavity Flows—Part 1: Cavities Forming on Models Without Spanwise Variation," J. Fluid Mech., **431**, pp. 1–41.
[24] Jakobsen, J. K., 1964, "On the Mechanism of Head Breakdown in Cavitating Inducers," ASME J. Basic Eng., **86**(2), pp. 291–305.
[25] Reisman, G. E., Wang, Y. C., and Brennen, C. E., 1998, "Observations of Shock Waves in Cloud Cavitation," J. Fluid Mech., **355**, pp. 255–283.
[26] Ganesh, H., Mäkiharju, S. A., and Ceccio, S. L., 2016, "Bubbly Shock Propagation as a Mechanism for Sheet-to-Cloud Transition of Partial Cavities," J. Fluid Mech., **802**, pp. 37–78.
[27] De Graaf, K., Brandner, P., and Pearce, B., 2017, "Spectral Content of Cloud Cavitation About a Sphere," J. Fluid Mech., **812**, pp. 1–13.
[28] Foeth, E. J., Van Doorne, C. W. H., Van Terwisga, T., and Wieneke, B., 2006, "Time Resolved PIV and Flow Visualization of 3D Sheet Cavitation," Exp. Fluids, **40**(4), pp. 503–513.
[29] Kawanami, Y., Kato, H., and Yamaguchi, H., 1998, "Three-Dimensional Characteristics of the Cavities Formed on a Two-Dimensional Hydrofoil," Third International Symposium on Cavitation, Vol. 1, Grenoble, France, Apr. 7–10, pp. 191–196.
[30] Zarruk, G. A., Brandner, P. A., Pearce, B. W., and Phillips, A. W., 2014, "Experimental Study of the Steady Fluid-Structure Interaction of Flexible Hydrofoils," J. Fluids Struct., **51**, pp. 326–343.
[31] Brandner, P. A., Lecoffre, Y., and Walker, G. J., 2007, "Design Considerations in the Development of a Modern Cavitation Tunnel," 16th Australasian Fluid Mechanics Conference, Gold Coast, Australia, Dec. 3–7, pp. 630–637.
[32] Pelz, P. F., Keil, T., and Groß, T. F., 2017, "The Transition From Sheet to Cloud Cavitation," J. Fluid Mech., **817**, pp. 439–454.